Magnetic Nozzle Radiofrequency Plasma Systems for Space Propulsion, Industry, and Fusion Plasmas*)

Kazunori TAKAHASHI[1,2,7], Christine CHARLES[3], Rod W BOSWELL[3], Kazuma EMOTO[4], Yoshinori TAKAO[4], Shiro HARA[5,6], Haruhisa NAKANO[7], Kenichi NAGAOKA[7] and Katsuyoshi TSUMORI[7]

[1] *Department of Electrical Engineering, Tohoku University, Sendai 980-8579, Japan*
[2] *Interdisciplinary Research Center for Non-equilibrium Plasma, Tohoku University, Sendai 980-8579, Japan*
[3] *Space Plasma, Power and Propulsion Laboratory, Research School of Physics, The Australian National University, Canberra ACT 2601, Australia*
[4] *Division of Systems Research, Yokohama National University, Yokohama 240-8501, Japan*
[5] *National Institute of Advanced Industrial Science and Technology, Tsukuba, Ibaraki 305-8506, Japan*
[6] *Minimal Fab Promoting Organization, Tsukuba, Ibaraki 305-8506, Japan*
[7] *National Institute for Fusion Science, Toki 509-5292, Japan*

(Received 4 January 2023 / Accepted 1 May 2023)

Low-pressure radiofrequency (rf) plasma sources have been widely used in various fields. When static magnetic fields are applied to these sources, a diverging magnetic field configuration known as a magnetic nozzle forms downstream of the source and interesting phenomena are observed. Such structures are frequently observed in space, e.g., the surface of the Sun and the geomagnetic fields. Here, the studies performed by the authors over the last decade on the fundamental plasma physics, the space plasma propulsion, the industrial plasma technology, and the radiofrequency ion source, are briefly overviewed. The design of sources based on the type of application is an important issue. Integrating a rf plasma source into a system often requires a compact and automatically controlled system, as presented here. Herein, interaction between the low-temperature plasmas and the hot fusion plasmas is sometimes mentioned in terms of "*Plasma Apparatus*."

© *2023 The Japan Society of Plasma Science and Nuclear Fusion Research*

Keywords: radiofrequency plasma, magnetic nozzle, space propulsion, Minimal Fab, ion source

DOI: 10.1585/pfr.18.2501050

1. Introduction

Low-pressure radiofrequency (rf) plasmas are typically classified into capacitively-, inductively-, and wave-coupled plasmas based on their heating mechanisms. The rf power from a generator is transferred to the load including the rf antenna/electrode and the plasma. A very efficient plasma production has been discovered when applying static magnetic fields to inductively coupled plasma sources. Because the helicon/whistler wave propagating in the magnetized plasmas contributes to efficient plasma production, the source invented by one of the authors is now well known as a helicon plasma source [1].

The rf plasma sources have greatly contributed to microelectronics, including semiconductor manufacturing and micro electro mechanical systems (MEMS), via various plasma processing, e.g., plasma etching, sputtering, chemical vapor deposition, ashing, and so on [2]. The heated electrons can create both chemically active species and charged ions in the plasmas; they play important roles in the processes. A noteworthy application of the rf plasma source is an ion beam source, which can be used for ion beam sputtering, ion milling, and secondary ion mass spectroscopy; some of authors have developed a commercial ion beam source [3].

The rf plasma source also has potential applications in space technology, e.g., a magnetic nozzle (MN) rf plasma thruster for space propulsion [4, 5]. The MN rf plasma thruster consists of an rf plasma source and a divergent magnetic field downstream of the source. By applying an axial magnetic field to the source, efficient power coupling can be often obtained by the helicon-wave-coupled mode; hence it is called a helicon thruster. The high-density plasma produced in the source is transported along the field lines to the source exit and spontaneously accelerated in the MN. When the accelerated plasma is ejected from the system, the reaction force is exerted on somewhere in the thruster structure and somehow, by which the spacecraft can be propelled in space.

The low-pressure rf plasma source plays a key role in the ion source for neutral beam injection (NBI) heating in fusion reactors [6]. As the plasma potential in the rf plasma source generally oscillates at rf frequency, both the beam

author's e-mail: kazunori.takahashi.e8@tohoku.ac.jp
*) This article is based on the presentation at the 31st International Toki Conference on Plasma and Fusion Research (ITC31).

© 2023 The Japan Society of Plasma Science and Nuclear Fusion Research

energy and the trajectories diverge, as observed in an industrial ion beam source [7]. To improve the ion source performance, the efficient plasma source is also an important topic.

Here the studies on these topics investigated by the authors are overviewed, i.e., the space plasma propulsion, the industrial plasma technology, and the ion source configuration, in Sections 2 - 4, respectively. These studies contain aspects of both physics and engineering. Therefore, the authors consider that the role of the newly established research department of '*Plasma Apparatus*' in the National Institute of Fusion Science would be valuable for further research and development.

2. Space Electric Propulsion

In typical electric propulsion devices, the gaseous propellant is ionized and energized by coupling electric power and exhausted into space [8]. Based on the law of momentum conservation, the thrust propelling a spacecraft is equal in magnitude and opposite in direction to the momentum exhausted from the system per unit time and is generally given by the sum of the static and dynamic pressures. In case of a typical helicon thruster, the electron temperature is much higher than the ion and neutral temperatures, providing negligible static pressures of the ions and the neutrals. Therefore, the thrust T is given by $T = \int (p_e + m_i n_p u_i^2)\, dA$, where A, n_p, u_i, and p_e denote the cross section of the fluid flow, plasma density, ion velocity, and electron pressure, respectively. By combining the direct measurement of the thrust and plasma diagnoses, one can find new insights into physics in addition to the assessment of the thruster performance [9, 10]. Figure 1 (a) shows the schematic of a typical MN rf plasma thruster, which consists of an rf plasma source and a MN. Examples of physical processes related to thruster development are summarized in Fig. 1 (a).

When the MN is applied to the rf plasma source, a current-free double layer (CFDL) and/or an ambipolar electric field are spontaneously formed near the thruster exit and in the MN. The electric fields electrostatically accelerate the ions in the upstream source, as observed in the ion energy distribution functions, as shown in Fig. 1 (b) [9, 11]. A number of experiments have validated the generation of the supersonic ion beam [12–17]. One-dimensional kinetics of the electrons have been revealed by measuring the electron energy probability functions (EEPFs) upstream and downstream of the CFDL as in Fig. 1 (c) [18–23]. The upstream EEPF shows a depleted tail at the break energy ε_{break} corresponding to the potential drop of the CFDL. The downstream EEPF is similar to the high-energy and low-temperature electrons in the upstream EEPF. These findings imply that electrons with an energy above ε_{break} are decelerated by and overcome the CFDL. Thus, it can be deduced that the accelerated ions are electrically neutralized by the electrons overcoming the CFDL, proposing that the system can be applied to neutralizer-free plasma thrusters.

The aforementioned electrostatic ion acceleration process converts the parallel electron pressure into an ion dynamic pressure while conserving the total axial momentum of the electrons and ions, i.e., the thrust is not changed. Alternatively, the axial momentum can be increased by a Lorentz force due to the plasma internal current and the radial magnetic field in the MN [24, 25]. This can be derived from the momentum equations of the ions and electrons, which are given as follows:

$$m_j \nabla \cdot (n_j \boldsymbol{v}_j \boldsymbol{v}_j) = q_j n_j (\boldsymbol{E} + \boldsymbol{v}_j \times \boldsymbol{B}) - \nabla p_j, \quad (1)$$

where j denotes the particle species. By considering the negligible electron inertial term and the ion pressure, the total thrust T_{total} can be summarized as $T_{total} = T_s + T_B + T_w$. The detailed expression of the three terms can be found in Ref. [26]. In this equation, T_s refers to the maximum electron pressure force exerted on a source back plate via ion acceleration in the sheath, where equal momentum is directed toward the source exit [27]. T_B refers to the Lorentz force due to the electron diamagnetic current and radial magnetic field, and T_w refers to the axial momentum lost

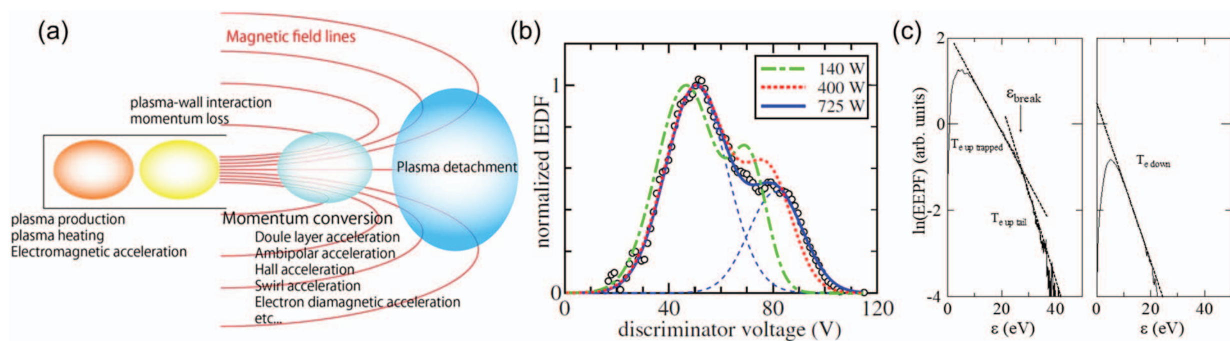

Fig. 1 (a) Typical configuration of MN rf plasma thruster and related physical processes. (b) Ion energy distribution functions measured in the MN [9]. *Reproduced with permission from Appl. Phys. Lett.* ***98****, 141503 (2011). Copyright 2011, American Institute of Physics.* (c) EEPFs measured (left) upstream and (right) downstream of a current-free double layer [18]. *Reproduced with permission from Phys. Plasmas 14, 114503 (2007). Copyright 2007, American Institute of Physics.*

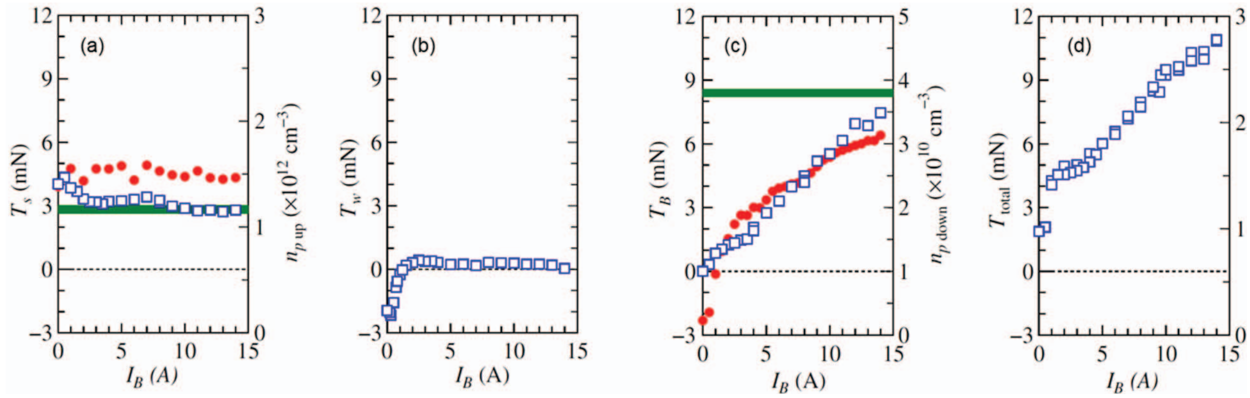

Fig. 2 Directly measured thrust components of (a) T_s, (b) T_w, and (c) T_B, and (d) the total thrust T_{total}. [28]. *Reproduced with permission from Phys. Rev. Lett.* ***110****, 195003 (2013). Copyright 2013, American Physical Society.*

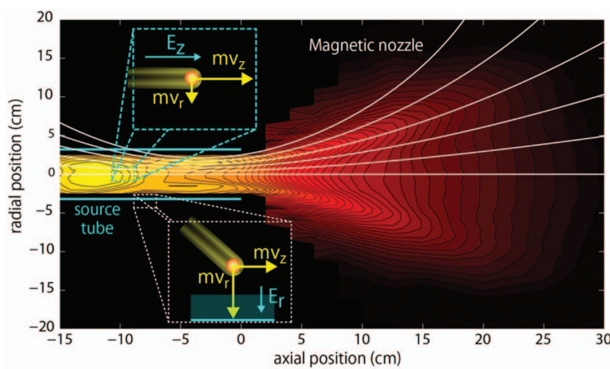

Fig. 3 Physical description of the axial momentum lost to the radial source wall. *Credit: Kazunori Takahashi.*

to the radial source wall [28]. These forces can be measured by attaching either the source back wall, the solenoid creating the MN, or the radial source wall to the pendulum thrust balance, as shown in Fig. 2, where the source plasma density is maintained at constant and the density in the MN is increased by increasing the magnetic field strength (solenoid current I_B), i.e., by inhibiting the cross-field diffusion in the MN. The total thrust T_{total} is also measured as a function of I_B by attaching all the components to the pendulum balance, as shown in Fig. 2 (d). T_s and T_w are nearly constant and close to zero, as shown in Figs. 2 (a) and 2 (b), respectively, while T_B increases with increasing magnetic field strength. Thus, T_B arising from the MN effect significantly contributes to thrust generation. A detailed measurement and analysis of the internal plasma current has been provided in Ref. [29]. The energy source of the thrust is the thermal energy of the electrons energized by the rf power. Therefore, the electron internal energy, i.e., the temperature, should decrease when they contribute to the thrust generation. As well as the kinetic discussion based on the EEPFs, thermodynamic analogies are important to understand and model the thrust imparted by the MN, as vigorously investigated in recent years [30–37].

Subsequent experiments have shown a non-negligible

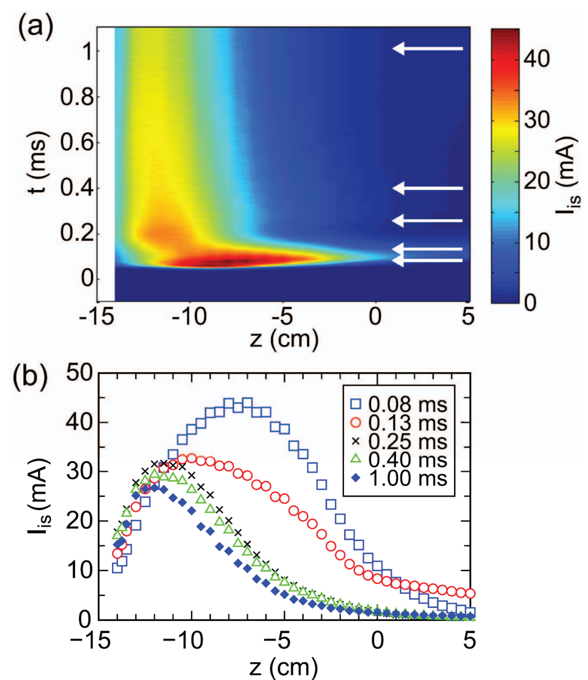

Fig. 4 (a) Temporal evolution of the axial profile of the ion saturation current I_{is} of the Langmuir probe. (b) Axial profiles of I_{is} at the representative time shown by the arrows in Fig. 4(a) [40]. *Reproduced with permission from Appl. Phys. Lett. 108, 074103 (2016). Copyright 2016, American Institute.*

axial force T_w onto the radial source wall for highly ionized plasmas with Kr and Xe propellants, where a strong density decay and a potential drop inside the source tube have been detected [38, 39]. When ions accelerated by the axial electric field inside the source are lost to the radial source wall, their axial momentum is transferred to the radial source boundary, as shown in Fig. 3. Such a structure is observed in Ar gas for high rf power cases, where the axial density peak temporally moves to the upstream side of the source, as seen in the spatiotemporal evolution of the density profile [Fig. 4]. Qualitative measurement has indi-

cates the significant decrease in the neutral density near the source exit [40], and this phenomenon is called neutral depletion. This observation has also been observed in previous studies [41–43]. The observed plasma density profile appears to be consistent with the analytical model incorporating the neutral depletion effect [44]. Such a density profile causing axial momentum loss can be improved by injecting the propellant gas near the thruster exit, resulting in increased thrust [45].

Energy flux lost to the wall (p_w) is given by the sum of the ion kinetic energy and the electron thermal energy (p_{we}) at the wall as:

$$p_w = \frac{1}{2}m_i(u_{rw}^2 + u_{zw}^2)n_s u_{rs} + p_{we}, \quad (2)$$

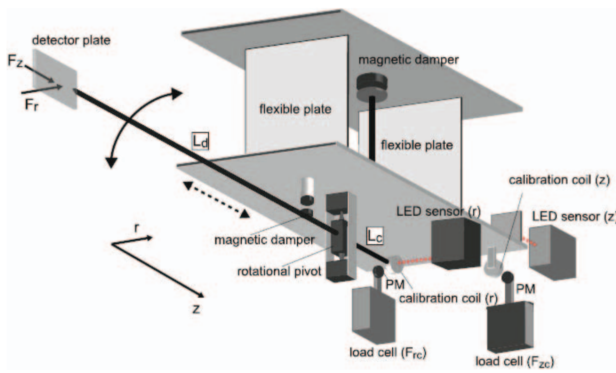

Fig. 5 Schematic diagram of momentum vector measurement instruments [48]. *Reproduced with permission from Sci. Rep.* ***10****, 1061 (2020). Copyright 2020, Authors, licensed under a Creative Commons Attribution (CC BY) License.*

where u_{rw}, u_{zw}, u_{rs}, and n_s denote the radial ion velocity at the wall, axial ion velocity at the wall, radial ion velocity at the sheath edge, and plasma density at the sheath edge, respectively. In the case of magnetized electrons, p_{we} would be close to zero. The energy loss can be rewritten by the axial (f_z) and radial (f_r) force densities exerted on the radial source wall and the ion saturation current density j_{is} of the Langmuir probe for unmagnetized and magnetized conditions, respectively, as shown below:

$$P_w = \frac{e}{2m_i}\frac{(1 + 2/5.2)f_r^2 + f_z^2}{j_{is}}, \quad (3)$$

$$P_w = \frac{e}{2m_i}\frac{f_r^2 + f_z^2}{j_{is}}. \quad (4)$$

The local force components f_r and f_z can be measured by a recently developed momentum vector measurement instrument shown in Fig. 5, where the axial and radial forces exerted on the detector plate surface can be transmitted to the axially movable pendulum and the rotatable pivot structure, respectively. The displacements for both cases are measured using displacement sensors [46, 47]. Figures 6 (a) - 6 (d) show the axial profiles of the energy fluxes lost to the wall, as estimated using Eqs. (3) and (4), corresponding to the upper and lower limits owing to the uncertainty of the models. The energy flux in the upstream region can be reduced by increasing the solenoid current. By integrating the data over the axial region of the measurement, the total power lost the radial wall P_w can be calculated as plotted by open and filled circles in Fig. 6 (e). The filled diamonds denote the power absorbed by the plasma, and the open and filled squares denote the ratio of P_w/P_{abs}. The energy lost to the wall can be reduced by increasing

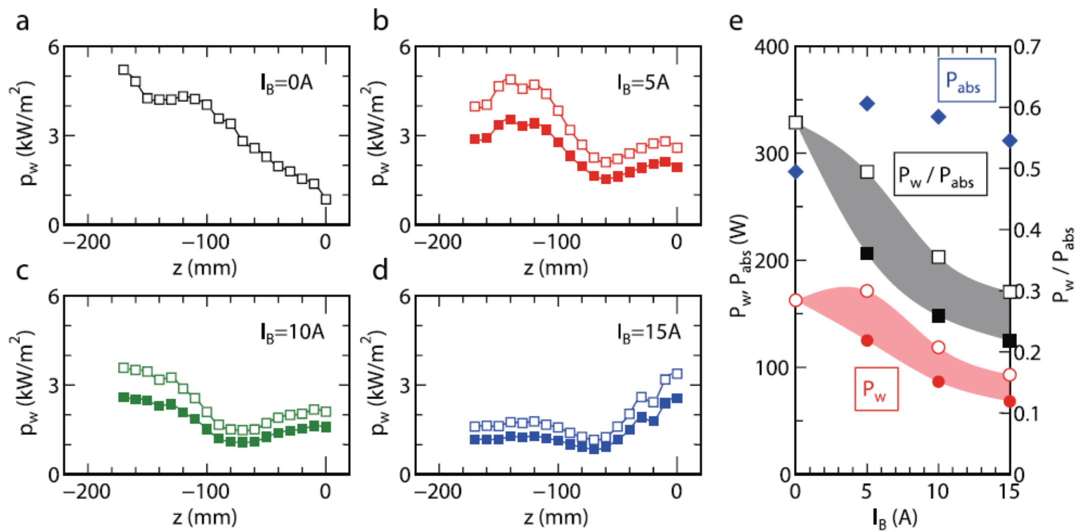

Fig. 6 Axial profiles of energy flux lost to the wall for (a - d) various solenoid currents, where open and filled squares are estimated from Eqs. (3) and (4), respectively, and solid lines are added as visual guides. (e) Total power P_w (open and filled circles), rf power P_{abs} absorbed by the plasma (filled diamonds), and ratio of P_w/P_{abs} (open and filled squares), as a function of the solenoid current I_B. Because the open and filled symbols in P_w and P_w/P_{abs} are the upper and lower limits of the estimation from Eqs. (3) and (4), respectively, the actual power loss would be within the colored regions [48]. *Reproduced with permission from Sci. Rep.* ***10****, 1061 (2020). Copyright 2020, Authors, licensed under a Creative Commons Attribution (CC BY) License.*

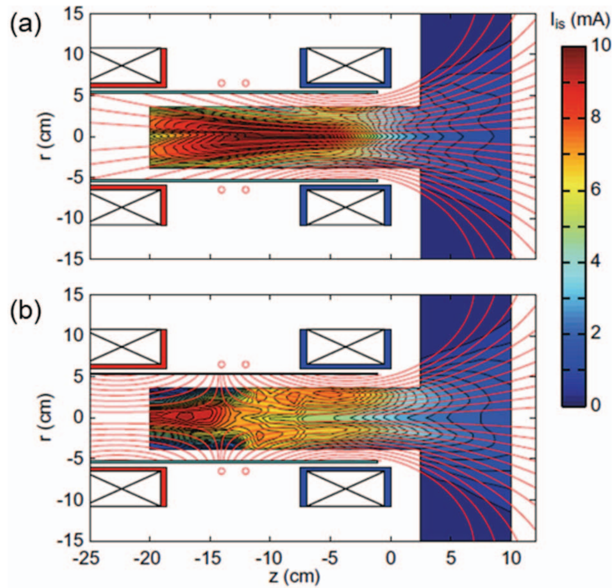

Fig. 7 Two-dimensional mapping (colored scale) of the ion saturation current I_{is} of the Langmuir probe for (a) I_{Bup} = 0 A and (b) I_{Bup} = −15 A, along with the calculated magnetic field lines. [51]. *Reproduced with permission from Sci. Rep. **12**, 18618 (2022). Copyright 2022, Authors, licensed under a Creative Commons Attribution (CC BY) License.*

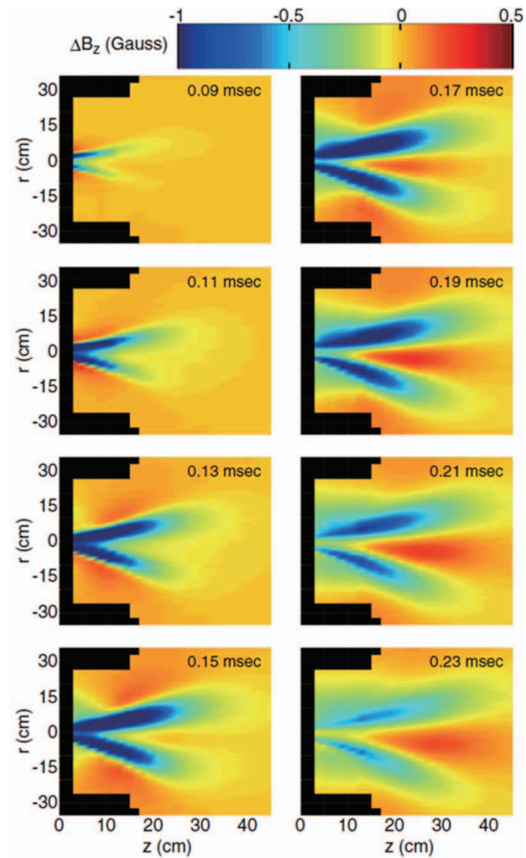

Fig. 8 Temporal evolution of two-dimensional mapping (colored scale) of the plasma-induced axial magnetic field ΔB_z. [62]. *Reproduced with permission from Phys. Rev. Lett. **118**, 225002 (2017). Copyright 2017, American Physical Society.*

the magnetic field strength. However, about 30% of the energy is still lost to the wall even if the solenoid current is increased up to 15 A (about 300 G magnetic field in the source) [48, 49].

One of the thruster experiments has shown the thruster efficiency approaching 20% [50]. To further decrease the energy loss to the wall, a cusp magnetic field has been applied upstream of the rf antenna, as shown in Fig. 7 while maintaining the MN structure downstream of the source [51]. A zero magnetic field region, i.e., the cusp, can be formed by supplying the opposite polarities for the upstream and downstream solenoid currents. The cusp geometrically isolates the plasma upstream of the rf antenna ($z < -15$ cm) from the source wall, thus reducing the plasma loss to the wall. The detected thrusts for 5 kW rf power in no-cusp [Fig. 7 (a)] and cusp [Fig. 7 (b)] conditions are approximately 60 mN and 80 mN, respectively, demonstrating the performance improvement by reducing the plasma loss to the wall. The estimated thruster efficiencies calculated from the rf power, measured thrust, and gas flow rate can be increased to about 30%, being the highest in this type of thruster [51].

The magnetic field lines form closed loops. Via the spontaneous acceleration and momentum conversion processes in the MN region, the plasma has to be finally deviated from the field lines; otherwise, the plasma will return to the thruster, providing no net thrust in space. This is well known as a plasma detachment problem. The ion Larmor radius downstream of the MN is typically larger than the plasma scale. Hence, unmagnetized ions can be deviated from the field lines, as observed in several experiments [52–55], while electrons remain magnetized. Several scenarios related to electron detachment have been proposed and investigated so far, e.g., magnetohydrodynamic (MHD) detachment [56], cross-field diffusion [57], and wave-driven detachment [58], where the latter two induce the outward diffusion and the resultant divergence of the plasma beam. Plasma detachment is frequently observed in space, e.g., plasma ejection from the surface of the Sun, where the plasma flow can take away its magnetic field. When considering the similar phenomena suggested by Arefiev and Breizman [56], the MN would be stretched, i.e., the axial component of the magnetic field would increase on the center axis of the MN, corresponding to $\Delta B_z > 0$. Although most of the laboratory experiments show the diamagnetic nature of the plasma, i.e., $\Delta B_z < 0$ [26, 28, 29, 59–61], the increase in ΔB_z has been observed further downstream while sustaining the diamagnetic signal near the thruster exit, as shown in Fig. 8 [62]. The observation seems to be consistent with the finding reported in Ref. [56], but the phenomenon occurs at an Alfvén Mach number of about 0.2 - 0.3, which is smaller

than generally thought. The interpretation of this discrepancy can be found in Ref. [62]. Since the change in the magnetic field is only about several percent of the applied one, further optimization will be required to induce the plasma detachment. The magnitude of the signal can be increased by increasing the rf power; the MHD detachment is expected to occur only in the high beta condition.

Alternatively, a recent experiment has demonstrated inward electron transport by a spontaneously excited wave with a frequency that is considerably higher than the ion cyclotron frequency but lower than the lower hybrid frequency [63]. Figure 9 shows the radial profile of the real part of the cross spectrum between density and velocity fluctuations, corresponding to the cross-field electron particle flux and indicating the inward flux. The electrons can radially climb up the density gradient near the plasma edge toward the main axis of the MN, which contributes to the neutralization of the ions deviating from the MN.

As described above, the elaborated experiments including the establishment of the setup, the accurate diagnoses, and the interpretations of the data, have significantly contributed to the discoveries and the understanding of the important physical processes so far. The numerical works have also been progressed with particle-in-cell simulations that have reproduced the axial momentum lost to the wall and the momentum conversion processes in the MN [64–66]. Developing an engineering model of the MN rf plasma thruster involves many challenging subjects, including the rf system, thermal design, endurance test, and lifetime test. For more high-power thruster, for example, collaboration between the thruster and fusion communities might be useful. The authors feel that these facts match the concept of the "*Plasma Apparatus Unit*" at the National Institute of Fusion Science.

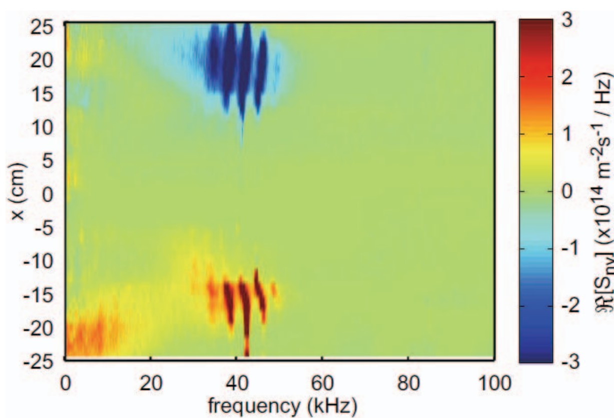

Fig. 9 Radial profile of the real part of the cross spectrum S_{nv} of the density and velocity fluctuations, where the positive and negative values correspond to the particle flux in the positive and negative x directions [63]. *Reproduced with permission from Sci. Rep.* ***12****, 20137 (2022). Copyright 2022, Authors, licensed under a Creative Commons Attribution (CC BY) License.*

3. Industrial Plasmas

Over the past several decades, low-cost production of semiconductor devices has been achieved by increasing wafer diameter, requiring a large-scale manufacturing system called "Mega Fab", which can provide only low-mix and high-volume products due to its facility scale and development cost. Plasma reactors have well contributed to the microfabrication and film deposition processes as already mentioned in the introductory part. "Minimal Fab" has been proposed and vigorously developed to establish a new industrial system that can provide high-mix and low-volume products in semiconductor and MEMS manufacturing [67–69]. Minimal Fab consists of various compact manufacturing tools to process a half-inch wafer, which is transferred between the tools via a localized clean wafer transfer system. Thus, it does not require a clean room for the fab and reduces the development and production costs for high-mix and low-volume products. Figure 10 shows a photograph of the minimal multi-target sputtering tool developed by some of authors [70]. All of the components composing each tool, e.g., a wafer transfer mechanics, a programmable controller, a vacuum chamber, a pumping system, a mass flow controller, AC-DC convertors, an rf plasma source, and an rf generator, have to be contained in a compact frame of 29.5 cm in width, 45 cm in depth, and 144 cm in height, which is standardized to connect the different processing tools. Therefore, the plasma sources for the plasma processing tools, e.g., the etching and sputtering reactors, have to be miniaturized.

In a traditional rf plasma source system, output rf power from a generator is transferred to a load via an impedance matching box consisting of two variable ca-

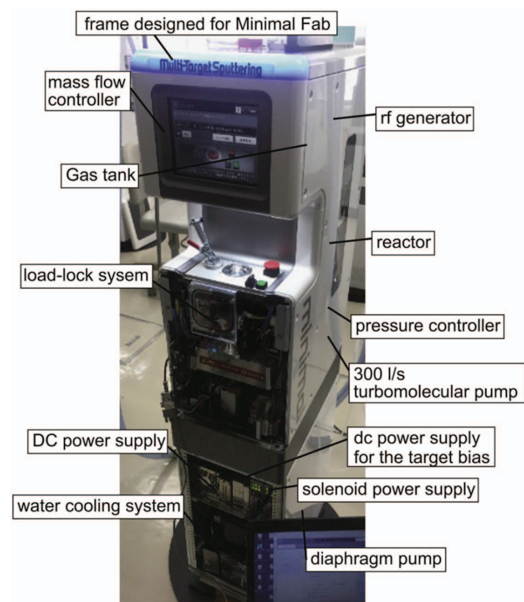

Fig. 10 Photograph of a minimal multi-target sputtering tool [70]. *Reproduced with permission from Vacuum* ***171****, 109000 (2020). Copyright 2020, Elsevier.*

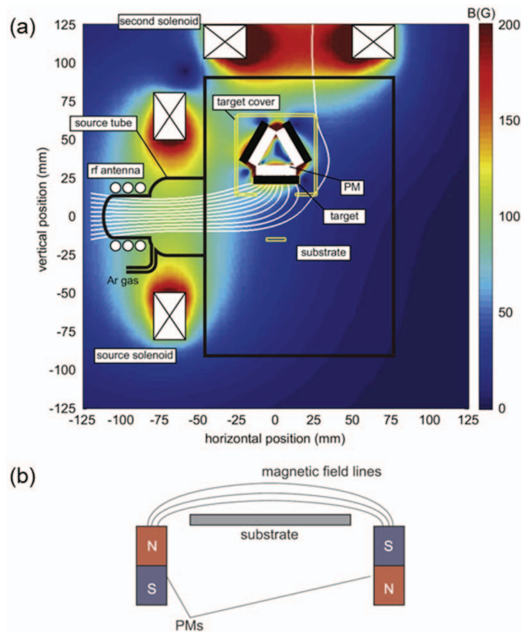

Fig. 11 (a) Schematic of a minimal multi-target sputtering tool. (b) Side view of the Si substrate and the magnetic filter [70]. *Reproduced with permission from Vacuum* ***171****, 109000 (2020). Copyright 2020, Elsevier.*

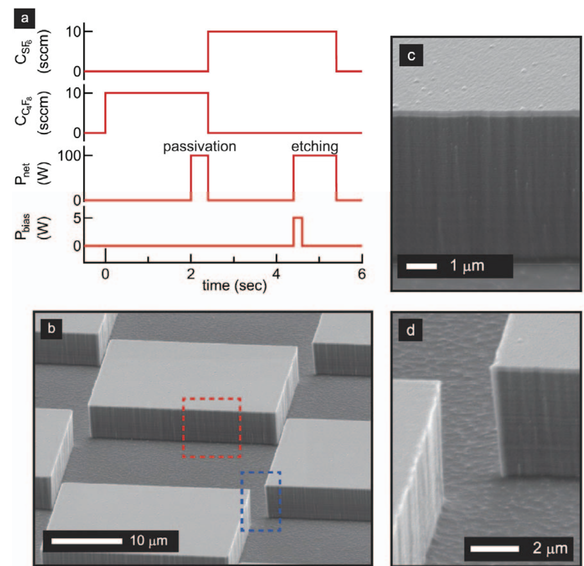

Fig. 12 (a) Temporal sequence of the Bosch process. (b - d) Typical SEM image of the etched silicon substrate, where 200-nm Al mask is formed prior to the etching process [77]. *Reproduced with permission from AIP Adv.* ***11****, 025013 (2021). Copyright 2021, Authors, licensed under a Creative Commons Attribution (CC BY) License.*

pacitors and an inductor (if needed) to match the load impedance to both the output impedance of the generator and the characteristic impedance of the power transfer line, being typically 50 Ω. The capacitance values are mechanically controlled, resulting in the massive structure and the slow response for impedance matching. Alternatively, impedance matching by using a variable frequency rf generator has been demonstrated [71, 72]. Here, the output frequency and power can be quickly and automatically controlled by mounting a controller board on the system, where tiny ceramic capacitors are used for the matching circuit [71]. One of the authors has demonstrated impedance matching within 5 ms and the stabilization of the discharge by maintaining not the output power but the net power, corresponding to the forward minus reflected powers, at a constant level [73, 74]. This system is indeed useful because of the tiny matching circuit for developing the sputtering and etching tools in Minimal Fab. Moreover, the rf system is useful for rf plasma thrusters, requiring a compact rf system for plasma production [75, 76].

In the minimal multitarget sputtering tool shown in Fig. 11 (a) [70], the plasma produced in the source is transported along the curved magnetic field lines to the negatively biased target surface, where the ions are accelerated by the sheath voltage. The ions accelerated by the sheath and impinging the target can sputter the target material and a thin film can be deposited on the substrate. The target material can be changed by rotating the shaft of the target holder, providing a multilayer thin film. Simultaneously, secondary electrons are ejected from the target surface and accelerated by the sheath voltage. A significant increase in substrate temperature up to about 350°C due to the accelerated secondary electrons was observed. To inhibit this unexpected substrate heating, a magnetic filter structure has been installed near the substrate, as shown in Fig. 11 (b), reducing the substrate temperature to less than 200°C.

A fast and automatically controlled frequency variable rf system is also mounted on a minimal silicon etching tool, which utilizes the Bosch process for deep silicon etching [77]. Because the etching and passivation gases are alternately switched, the plasma is synchronized with the gas switching. Therefore, the impedance has to be matched within a time much less than the plasma pulse width, where the plasma pulse width is desired to be reduced less than 1 sec, since the size of the scallop structure on the etched sidewall depends on the pulse width of the etching. Figure 12 (a) shows the typical temporal sequence of the Bosch process, and Figs. 12 (b - d) show the SEM images of the etched silicon wafer. As shown, the scallop size on the sidewall is invisible, facilitating the nearly vertical etching.

As mentioned before, the authors have developed the minimal sputtering and etching tools over the last several years. In the development, the various plasma technologies have been utilized. The authors have found that there are various common technologies and insights with the plasma thruster development (the rf plasma source, the rf system, the magnetic nozzle) and fusion technology (magnetic filter), while it still requires the high-level design and lowering the cost for practical use, where the authors would like

to thank some companies working together.

4. Fusion-Relevant Plasmas

Plasma heating is one of the most important technologies for magnetically confined fusion plasma reactors. Presently, an NBI system utilizing a negative ion source is the primary source for plasma heating, where the negative hydrogen/deuterium ions are extracted from the low-temperature plasma source and accelerated by the electrodes; the ion beam is neutralized in a gas neutralizer. The negative ion source using a filamented arc discharge has been well established and plays an important role in the fusion plasma studies [78]. As ITER requires a long-pulsed and high-power operation, the filamented source is planned to be replaced by an inductively coupled rf plasma source [6].

An experimental setup with a helicon source terminated by a magnetic filter and beam extraction grids has been established, as shown in Fig. 13 (a), where the source field lines are rapidly bent owing to the presence of the magnetic filter [79]. The measurement of the EEPFs along the axis have shown that the effective electron temperature is locally increased between the source exit and the magnetic filter as seen in Fig. 13 (b). The measurement of the wave magnetic fields indicates the presence of a standing wave in the high-temperature region, i.e., the helicon wave is reflected by the magnetic filter, where the bent magnetic fields drastically changed the refractive index for the wave. Therefore, the low electron temperature due to the magnetic filter is still maintained by excluding the wave from the magnetic filter region [Fig. 13 (b)]. It can be deduced that the high-temperature region for ionization/excitation and the low-temperature region for negative ion production can coexist at a relatively near distance, which may be advantageous to the negative ion source.

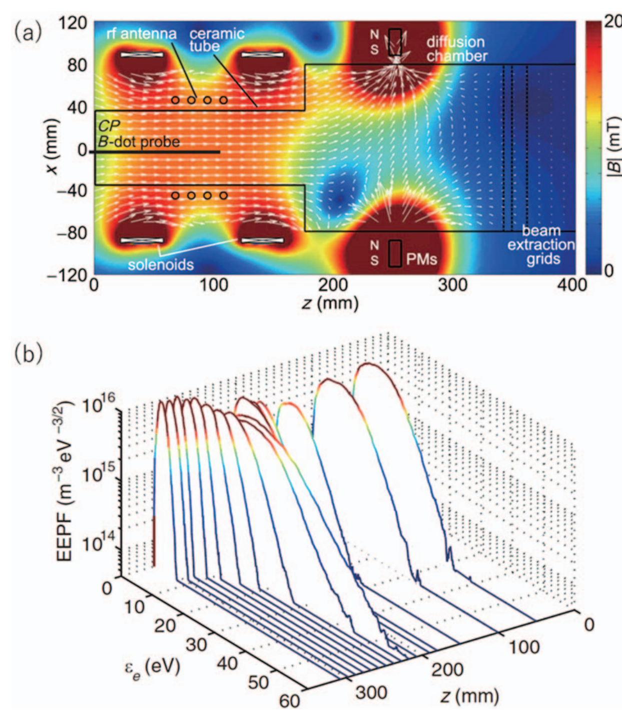

Fig. 13 (a) Experimental setup for the helicon source terminated by the magnetic filter and the beam extraction grids. (b) EEPFs along the center axis. [79]. *Reproduced with permission from Phys. Rev. Lett.* ***116****, 135001 (2016). Copyright 2016, American Physical Society.*

In rf plasma sources, the plasma potential generally oscillates at the rf frequency and its harmonics; it is expected that the potential structure near the beam extraction grids spatiotemporally oscillates as well. The curvature of the equipotential plane would significantly affect beam divergence as well as energy spread. This has been verified by artificially superimposing the oscillating potential on the filamented source plasma in the positive ion beam source, where the spatiotemporal profile of the ion beam current downstream of the grids has been measured as shown in Fig. 14 [80]. No visible oscillation at the beam core has been detected, while the beam current in the peripheral region (sometimes called a '*beam halo*') is found to oscillate by the rf potential oscillation. This observation indicates that only the curvature of the equipotential lines near the hole edge of the extraction grid temporally oscillates for the positive ion beam source. The oscillation of the beam divergence in the negative ion beam source has also been observed and investigated in detail in a Research-and-Development Negative Ion Source in NIFS [81], indicating the importance of source plasma stability. More recently, oscillation in the rf negative ion source has been observed; control of the rf potential oscillation may be required for the performance improvement of the rf negative ion source [82, 83].

5. Summary

In summary, this research work presents an overview of the studies on rf plasma sources related to space propulsion, industrial plasma reactors, and fusion-relevant plasmas and provides fruitful insights obtained over the last decade via domestic and international collaborations. These studies contain the fundamental physics, plasma applications, and engineering issues for plasma production, control, and peripheral components. In addition, this study presents examples of the common technologies for different plasmas, e.g., the compact rf generator for propulsion and industrial plasmas and the magnetic filter for negative ion sources and industrial plasmas. In the authors' understanding, the '*Plasma apparatus unit*' in NIFS will contribute to establish the comprehensive academic and industrial research including both science and technology. Further, the high-power plasma heating techniques may be useful for considerably high-power electric propulsion in the far future, which would be a good collaboration change between the low-temperature and high-temperature plasma communities.

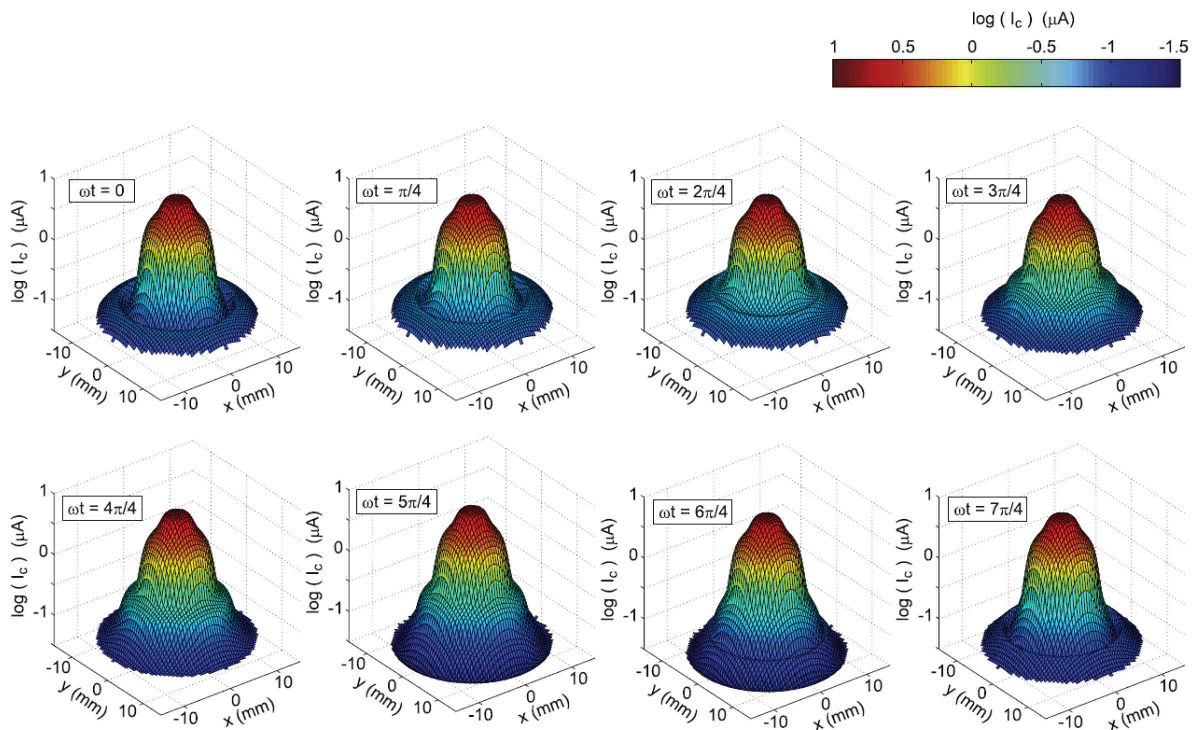

Fig. 14 Spatiotemporal profile of the positive ion beam current, where the profile is artificially prepared from the measured radial profile assuming the axisymmetric profile. *Reproduced with permission from New J. Phys.* ***21****, 093043 (2019). Copyright 2019, Authors, licensed under a Creative Commons Attribution (CC BY) License.*

Author Contribution

The laboratory experiments for the plasma thruster studies (Sec. 2) have been performed by Takahashi, Charles, and Boswell. Numerical simulations of the magnetic nozzle plasma thruster have been mainly performed by Emoto and Takao as a collaboration with Takahashi. Takahashi have developed the minimal multi sputtering and etching tools and Hara have performed comprehensive organization of Minimal Fab (Sec.3). Takahashi, Nakano, Nagaoka, and Tsumori have performed the studies on the ion beam source (Sec.4). The manuscript written by Takahashi was reviewed by all the authors.

Acknowledgments

K. Takahashi would like to thank his students, i.e., Mr. Chiba, Mr. Sugawara, Mr. Saito, Mr. Hanaoka, Mr. Takayama, and Mr. Imagi, for their help in the experiments related to Fig. 3, Fig. 6, Fig. 11, Fig. 12, and Fig. 13, respectively.

This work is partially supported by Grant-in-Aid for Scientific Research (Grant Nos. 19H00663 and 23H05442) from the Japan Society for the Promotion of Science and Fusion Oriented REsearch for disruptive Science and Technology (FOREST) from Japan Science and Technology Agency (Grant No. JPMJFR212A).

[1] R.W. Boswell, Phys. Lett. **33A**, 457 (1970).
[2] M.A. Lieberman and A.J. Lichtenberg, *Principles of Plasma Discharges and Materials Processing, 2nd edn.* (Wiley, New York, 2005).
[3] http://www.oregon-physics.com/hyperion1.php
[4] C. Charles, J. Phys. D: Appl. Phys. **42**, 163001 (2009).
[5] K. Takahashi, Rev. Mod. Plasma Phys. **3**, 3 (2019).
[6] U. Fantz *et al.*, Front. Phys. **9**, 709651 (2021).
[7] N.S. Smith *et al.*, J. Vac. Sci. Technol. B, **24**, 2902 (2006).
[8] D.M. Goebel and I. Katz, *Fundamentals of Electric Propulsion: Ion and Hall Thrusters* (Wiley, Hoboken, 2008).
[9] K. Takahashi *et al.*, Appl. Phys. Lett. **98**, 141503 (2011).
[10] C. Charles *et al.*, Appl. Phys. Lett. **100**, 113504 (2012).
[11] C. Charles, Plasma Sources Sci. Technol. **16**, R1 (2007).
[12] X. Sun *et al.*, Phys. Rev. Lett. **95**, 025004 (2005).
[13] O. Sutherland *et al.*, Phys. Rev. Lett. **95**, 205002 (2005).
[14] M.A. Lieberman and C. Charles, Phys. Rev. Lett. **97**, 045003 (2006).
[15] I.A. Biloiu *et al.*, Appl. Phys. Lett. **92**, 191502 (2008).
[16] K. Takahashi *et al.*, Plasma Sources Sci. Technol. **19**, 025004 (2010).
[17] C. Charles *et al.*, Plasma Sources Sci. Technol. **19**, 045003 (2010).
[18] K. Takahashi *et al.*, Phys. Plasmas **14**, 114503 (2007).
[19] K. Takahashi *et al.*, Phys. Plasmas **15**, 074505 (2008).
[20] K. Takahashi *et al.*, Appl. Phys. Lett. **94**, 191503 (2009).
[21] C. Charles, Appl. Phys. Lett. **96**, 051502 (2010).
[22] K. Takahashi *et al.*, Phys. Rev. Lett. **107**, 035002 (2011).
[23] R.W. Boswell *et al.*, Front. Phys. **3**, 14 (2015).
[24] A. Fruchtman, Phys. Rev. Lett. **96**, 065002 (2006).
[25] E. Ahedo and M. Merino, Phys. Plasmas **17**, 073501 (2010).
[26] K. Takahashi *et al.*, Phys. Rev. Lett. **107**, 235001 (2011).
[27] T. Lafleur *et al.*, Phys. Plasmas **18**, 080701 (2011).

[28] K. Takahashi *et al.*, Phys. Rev. Lett. **110**, 195003 (2013).
[29] K. Takahashi *et al.*, Plasma Sources Sci. Technol. **25**, 055011 (2016).
[30] J.P. Sheehan *et al.*, Plasma Sources Sci. Technol. **23**, 045014 (2014).
[31] Y. Zhang *et al.*, Phys. Rev. Lett. **116**, 025001 (2016).
[32] J.M. Little and E.Y. Choueiri, Phys. Rev. Lett. **117**, 225003 (2016).
[33] M. Merino and E. Ahedo, IEEE Trans. Plasma Sci. **43**, 244 (2015).
[34] Y. Zhang *et al.*, Astrophys. J. **829**, 10 (2016).
[35] K. Takahashi *et al.*, Phys. Rev. Lett. **120**, 045001 (2018).
[36] J.Y. Kim *et al.*, New J. Phys. **20**, 063033 (2018).
[37] K. Takahashi *et al.*, Phys. Rev. Lett. **125**, 165001 (2020).
[38] K. Takahashi *et al.*, Phys. Rev. Lett. **114**, 195001 (2015).
[39] K. Takahashi *et al.*, Plasma Phys. Control. Fusion **59**, 054007 (2017).
[40] K. Takahashi *et al.*, Appl. Phys. Lett. **108**, 074103 (2016).
[41] A.W. Degeling *et al.*, Phys. Plasmas **6**, 3664 (1999).
[42] A.M. Keesee and E.E. Scime, Plasma Sources Sci. Technol. **16**, 742 (2007).
[43] A. Okamoto *et al.*, Phys. Plasmas **10**, 2211 (2003).
[44] A. Fruchtman, IEEE Trans. Plasma Sci. **36**, 403 (2008).
[45] K. Takahashi *et al.*, Appl. Phys. Lett. **109**, 194101 (2016).
[46] K. Takahashi *et al.*, AIP Adv. **8**, 105117 (2018).
[47] T. Sugawara *et al.*, Plasma Fusion Res. **14**, 1301143 (2019).
[48] K. Takahashi *et al.*, Sci. Rep. **10**, 1061 (2020).
[49] K. Takahashi *et al.*, Phys. Plasmas **27**, 064504 (2020).
[50] K. Takahashi, Sci. Rep. **11**, 2768 (2021).
[51] K. Takahashi, Sci. Rep. **12**, 18618 (2022).
[52] W. Cox *et al.*, Appl. Phys. Lett. **93**, 071505 (2008).
[53] C. Charles *et al.*, Phys. Rev. Lett. **103**, 095001 (2009).
[54] K. Terasaka *et al.*, Phys. Plasmas **17**, 072106 (2010).
[55] K. Takahashi *et al.*, J. Phys. D: Appl. Phys. **44**, 015204 (2011).
[56] A.V. Arefiev and B.N. Breizman, Phys. Plasmas **12**, 043504 (2005).
[57] E.B. Hooper, J. Propul. Power **9**, 757 (1993).
[58] S. Hepner *et al.*, Appl. Phys. Lett. **116**, 263502 (2020).
[59] R.L. Stenzel and J.M. Urrutia, Phys. Plasmas **7**, 4450 (2000).
[60] C.S. Corr and R.W. Boswell, Phys. Plasmas **14**, 122503 (2007).
[61] S. Shinohara *et al.*, Phys. Plasmas **23**, 122108 (2016).
[62] K. Takahashi *et al.*, Phys. Rev. Lett. **118**, 225002 (2017).
[63] K. Takahashi *et al.*, Sci. Rep. **12**, 20137 (2022).
[64] Y. Takao and K. Takahashi, Phys. Plasmas **22**, 113509 (2015).
[65] K. Emoto *et al.*, Phys. Plasmas **28**, 093506 (2021).
[66] K. Emoto *et al.*, Plasma Sources Sci. Technol. **30**, 115016 (2021).
[67] S. Khumpuang and S. Hara, IEEE Trans. Semicond. Manuf. **28**, 393 (2015).
[68] S. Khumpuang *et al.*, IEEE Trans. Semicond. Manuf. **28**, 551 (2015).
[69] Y. Liu *et al.*, Jpn. J. Appl. Phys. **57**, 06HD03 (2018).
[70] K. Takahashi *et al.*, Vacuum **171**[67 - 69], 109000 (2020).
[71] C. Charles *et al.*, J. Phys. D: Appl. Phys. **46**, 365203 (2013).
[72] K. Takahashi *et al.*, J. Phys. D: Appl. Phys. **50**, 265201 (2017).
[73] K. Takahashi *et al.*, Front. Phys. **7**, 227 (2020).
[74] K. Hanaoka *et al.*, IEEE Trans. Plasma Sci. **48**, 2138 (2020).
[75] C. Charles *et al.*, J. Propul. Power **30**, 1117 (2014).
[76] K. Takahashi and K. Hanaoka, Front. Phys. **9**, 639010 (2021).
[77] K. Hanaoka and K. Takahashi, AIP Adv. **11**, 025013 (2021).
[78] K. Tsumori *et al.*, Rev. Sci. Instrum. **81**, 02B117 (2010).
[79] K. Takahashi *et al.*, Phys. Rev. Lett. **116**, 135001 (2016).
[80] K. Takahashi *et al.*, New J. Phys. **21**, 093043 (2019).
[81] Y. Haba *et al.*, Jpn. J. Appl. Phys. **59**, SHHA01 (2020).
[82] M. Wada *et al.*, Rev. Sci. Instrum. **91**, 013330 (2020).
[83] T. Shibata *et al.*, AIP Conf. Proc. **2373**, 050002 (2021).